Mechanical and Thermal Management Characteristics of Ultrahigh Surface Area Single-Walled Carbon Nanotube Aerogels

*Kyu Hun Kim, Youngseok Oh, and Mohammad F. Islam**

Lightweight aerogels with large specific surface area (SSA) have numerous applications. Free-standing aerogels are created from single-walled carbon nanotubes (SWCNTs), and their SSA and pore characteristics, electrical conductivity, mechanical properties, and thermal management attributes are determined. The SSA of the aerogels is extraordinarily high and approaches 1291 $m^2 g^{-1}$ at a density of 7.3 mg mL^{-1}, which is close to the theoretical limit (≈1315 $m^2 g^{-1}$). Mechanical characterization shows that these aerogels have open-cell structures and their Young's moduli are higher than other aerogels at comparable density. The aerogels also enhance heat transfer in a forced convective process by ≈85%, presumably due to their large porosity and surface area.

1. Introduction

Electrically and thermally conducting lightweight materials with large specific surface area (SSA) have broad applications as composite fillers,[1,2] sieves,[3] heat sinks,[4] electrodes[5] and catalyst supports.[6] The properties of these foams are a function of cell geometry as well as the volume fraction and the intrinsic material properties of the cell walls.[7,8] As a result, foams created from a low volume fraction of strong, highly electrically and thermally conductive materials are optimal for these applications. Single-walled carbon nanotubes (SWCNTs) are anisotropic macromolecules with low density, ultrahigh SSA,[9] large mechanical strength[10] and exceptional conductivities, both electrical[11] and thermal.[12] SSA for individual SWCNTs with closed-ends[9,13] has been predicted to be ≈1315 $m^2 g^{-1}$ and ≈1600 $m^2 g^{-1}$ for SWCNTs with open-ends.[14–16] Consequently, different methodologies have been developed to utilize SWCNTs as cell walls in electrically and thermally conducting foams with large SSA.

Perhaps the most straightforward method of manufacturing SWCNT-based foams is a single-step chemical vapor deposition (CVD) process in which hundreds of micrometers to centimeters long (aspect ratio >100 000) SWCNTs form cellular structures during the growth process.[17] This method has predominantly been utilized to create foams with multi-walled CNTs (MWCNTs)[18–21] and a mixture of MWCNTs and SWCNTs.[22] However, MWCNTs have much lower SSA[9,13] and inferior physical properties compared to SWCNTs.[12] Also, due to the nature of CVD-based fabrication method, there are limitations in foam shapes, control of SWCNT types, and these materials contain impurities from synthesis. The SSA of SWCNT-based foams produced with this methodology[17] is much smaller than the SSA of individual SWCNTs.[9,13]

In another approach, we assembled purified CNTs to create free standing aerogel monoliths.[23] The solution processed CNTs had much shorter lengths of ≈1 μm (aspect ratio ≈1000) and contained a mixture of SWCNTs and MWCNTs. The CNT aerogel monolith fabrication is a multistep method involving isolation of CNTs in water using dispersants,[24] densification of CNT suspensions to form hydrogels composed of three-dimensional (3D) network of CNTs,[25,26] and removal of surfactant from these hydrogels and finally critical-point drying (CPD) of hydrogels.[23] These CNT aerogels have tunable shapes and sizes arising from the inherent flexibility of aerogel synthesis.[23] Also, the solution based manipulation of CNTs allows removal of impurities and sorting by length, diameter and electronic properties. These aerogels hold their shapes primarily via van der Waals interactions at discrete CNT crosslinking points or "nodes",[25] making them very fragile under stress.[23] Unfortunately, fabrication of aerogels from SWCNTs have not yet been possible because SWCNT hydrogels are typically too fragile and often disintegrate during the surfactant removal or the CPD steps.

In this paper, we report fabrication of low density, free standing aerogel monoliths from purified and isolated SWCNTs. We determined their SSA, which approached the theoretical limit, and pore characteristics including pore volume, pore radii and pore radii distributions. We further characterized their electrical, mechanical and thermal management properties. The Young's moduli of these aerogels were larger than any other aerogels at comparable density. These aerogels enhanced heat transfer in a forced convective cooling process by ≈85%, which we attribute to their large porosity and SSA.

K. H. Kim, Dr. Y. Oh, Prof. M. F. Islam
Department of Materials Science & Engineering
5000 Forbes Avenue
Carnegie Mellon University
Pittsburgh, PA 15213-3890, USA
E-mail: mohammad@cmu.edu

DOI: 10.1002/adfm.201201055

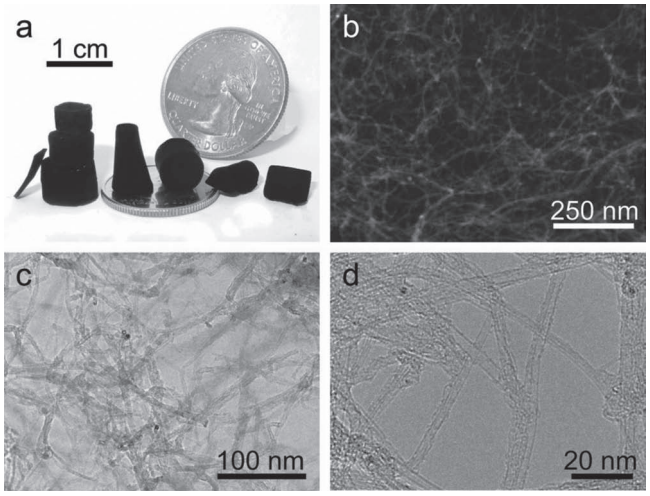

Figure 1. Images of SWCNT aerogels. a) Our fabrication method allowed production of aerogels in various sizes and shapes, such as cylinders, rectangles, cubes, truncated cylinders, and truncated cones. b) An SEM image of an aerogel cross-section showing networks of nanotubes. c) Low and d) high resolution TEM images show that the network composed of mostly isolated and entangled nanotubes.

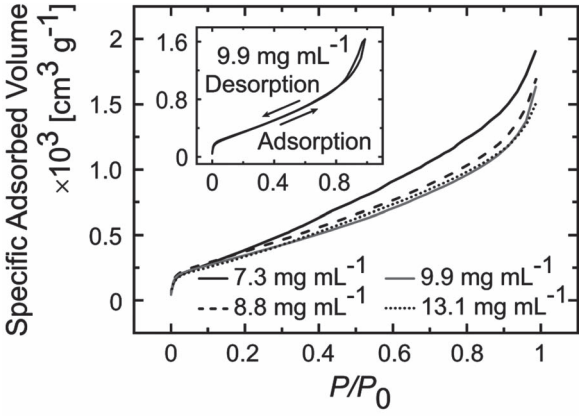

Figure 2. Adsorption isotherms. Nitrogen adsorption isotherms at 77 K were measured using cylindrical aerogels with mass densities ranging from 7.3 mg mL^{-1} to 13.1 mg mL^{-1}. The inset shows a representative adsorption-desorption isotherm with hysteresis loops for $P/P_0 > 0.8$ obtained from aerogel of density 9.9 mg mL^{-1}.

2. Results and Discussion

2.1. Images of SWCNT Aerogels

Photographs of free-standing aerogels of various shapes and sizes, fabricated by filling appropriate molds with the hydrogel precursor,[25,26] are shown in **Figure 1**a. The ability to tune shapes and sizes is a tremendous strength of our aerogel fabrication method. We imaged the nanotube network within the aerogels using scanning and transmission electron microscopy (SEM and TEM, respectively). High resolution SEM imaging of aerogel cross-sections showed a porous, isotropic nanotube network with an open-cell structure (Figure 1b), which was confirmed by low- and high-resolution TEM imaging (Figure 1c,d). TEM imaging also showed a few bundles of nanotubes (in Figure 1d), likely an artifact of sample preparation for TEM imaging which involved powdering of aerogels, dispersing in ethanol and then spraying onto a TEM grid. We note that SEM and TEM images did not reflect the actual pore structures within these aerogels because of the 2D representation of the depth of field in these microscopy techniques.

2.2. Characterization of SSA, Pore Volumes, Pore Sizes, and Pore Size Distribution of SWCNT Aerogels

We determined the SSA, pore volumes (V), pore radii (r), and the pore radii distributions for aerogels with density ρ = 7.3–13.1 mg mL^{-1} using the Brunauer-Emmett-Teller (BET) surface area measurement method.[27] In **Figure 2**, we show nitrogen adsorption isotherms at 77 K by plotting experimentally measured specific adsorbed volume (i.e., adsorbed volume divided by mass of the sample) versus relative pressure P/P_0 for cylindrical aerogels at different ρ; here, P is the equilibrium pressure and P_0 is the saturation pressure of the adsorbates at the adsorption temperature 77 K. Specific adsorbed volume of nitrogen slightly decreased with an increase in ρ, possibly from some bundling between nanotubes at higher concentrations. The adsorption-desorption isotherms showed hysteresis loops at $P/P_0 > 0.8$ which suggested that the isotherms are of Type IV under IUPAC (1972) classification,[28] and that the aerogels have mesopores, i.e., pores with diameters in the range of 2–50 nm;[28] a representative adsorption-desorption isotherm for an aerogel with ρ = 9.9 mg mL^{-1} is shown in the inset of Figure 2. Additionally, the isotherms did not show excessive nitrogen uptake for $P/P_0 < 0.05$,[14] suggesting an absence of micropores (i.e., pores with diameters <2 nm), or a sharp increase near P/P_0 = 1 suggesting an absence of macropores (i.e., pores with diameters >50 nm) in the aerogels.[14] The isotherms also showed a gradual increase in nitrogen adsorption for $P/P_0 > 0.05$ due to multilayer formation on nanotubes in the aerogels.

Next we determined SSA for aerogels with various ρ by analyzing the measured nitrogen adsorption isotherms using the BET theory[27] (**Figure 3**a and Supporting Information Figure S1). We first generated BET plots of $1/(W[(P_0/P) - 1])$ versus P/P_0 based on measured adsorption isotherms (Supporting Information Figure S1) and then fit a linear regression over a P/P_0 range of 0.04–0.11 to obtain the y-intercept $i = 1/(W_mC)$ and the slope $s = (C - 1)/(W_mC)$; W was the mass of adsorbed nitrogen at a relative pressure P/P_0 per unit sample mass, W_m was the mass of the adsorbed nitrogen monolayer per unit sample mass and C was the BET constant. We then calculated SSA from W_m: $SSA = (W_mN_AA_{CS})/M_w$, where $W_m = 1/(i + s)$, N_A was the Avogadro's number, A_{CS} was the cross-sectional area of nitrogen atoms and M_w was the molecular weight of nitrogen, as shown in Figure 3a. SSA increased with a decrease in ρ because of smaller specific adsorbed volume of nitrogen at higher ρ and reached 1291 m^2 g^{-1} for aerogels with ρ = 7.3 mg mL^{-1} which is very close to theoretical limit for SWCNTs with closed-ends[9,13] (1315 m^2 g^{-1}) identified with a dashed line in Figure 3a. We note that the optical and electrical conducting properties of the nanotubes in

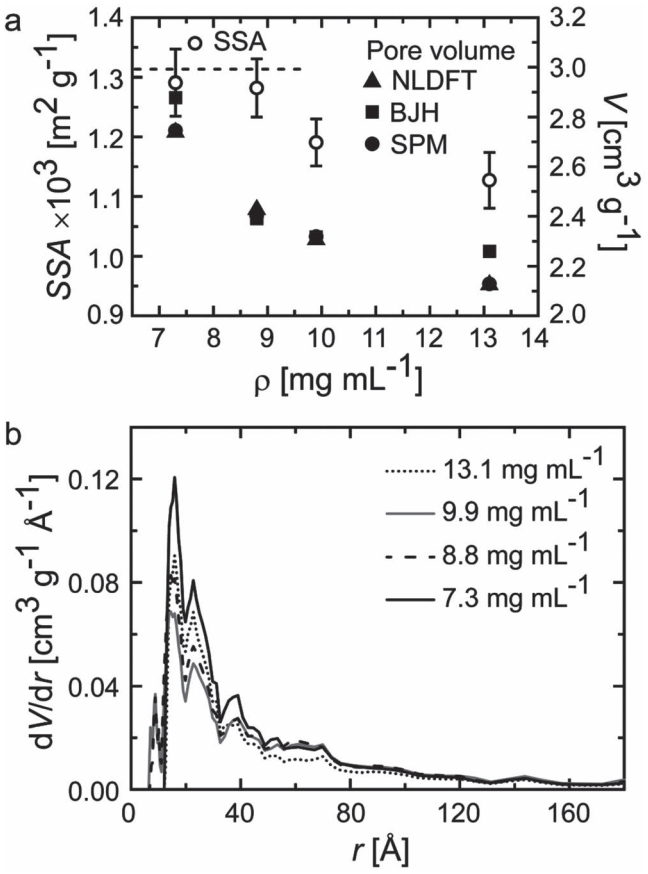

Figure 3. Specific surface area (SSA), pore volume (V), pore radii (r), and the distribution of pore radii (dV/dr) in the aerogels. a) SSA and V increased with a decrease in ρ. b) dV/dr based on the NLDFT analysis method. dV/dr determined using the BJH method is shown in Supporting Information Figure S2.

the aerogels were similar to those of "pristine" nanotubes (see Experimental Section), leading us to believe that the aerogel fabrication process did not damage the nanotubes, and the nanotubes had closed ends. We also measured SSA of nanotube aerogels (density 9.6 mg mL^{-1}) after annealing them at 1100 °C for 12 h in vacuum (1136 m^2 g^{-1}), which would have repaired any damage to nanotubes, and found it to be similar to the SSA of aerogels with similar density (9.9 mg mL^{-1}) before annealing (1191 m^2 g^{-1}), additionally confirming that the nanotubes did not open-up during aerogel fabrication process.

We then characterized r, V and pore radii distribution for the aerogels from the isotherms using two different methods: the non-local density functional theory (NLDFT) method[29] and the Barret, Joyner and Halenda (BJH) method;[30] V was additionally determined using the single point method (SPM).[31] Note, to determine V and pore radii distribution using the BJH method, we used the desorption regime of the isotherm, which represents the lower free energy state compared to the adsorption regime of the isotherm.[30] We show the range and distribution of pore radii by plotting the fraction of pore volume (dV/dr) as a function of r for aerogels with four different ρ obtained using NLDFT analysis in Figure 3b and BJH method in Supporting Information Figure S2. Both the NLDFT and BJH methods fit the isotherms well with fitting errors ≈3% and provided similar dV/dr. However, the NLDFT analysis suggested that the aerogels had mostly mesopores with ≤3 vol% of micropores, particularly for aerogels with ρ = 8.8 and 9.9 mg mL^{-1}, whereas BJH method indicated that all the pores in the aerogels at any ρ were mesopores. The pore radii were larger in lower density samples and r decreased with an increase in ρ, presumably due to higher packing of nanotubes within the aerogel.[26] Further, the accuracy of the isotherm fitting by both the NLDFT method, which assumes slit-like pores, and BJH method, which assumes cylindrical pores, suggested that the pores had non-spherical shapes. The pore volume calculated from NLDFT, BJH and SPM were similar (Figure 3), and the largest V was ≈2.8 cm^3 g^{-1} at ρ = 7.3 mg mL^{-1}.

2.3. Electrical and Mechanical Properties of SWCNT Aerogels

The aerogel fabrication process did not damage the electrical transport properties of nanotubes. The electrical conductivity, κ, of aerogels with ρ = 7.3 mg mL^{-1} was 23 S m^{-1} and increased linearly to 71 S m^{-1} at ρ = 14.1 mg mL^{-1} (**Figure 4**a). κ of these aerogels was lower than typical values of other CVD-grown SWCNT foams.[17] We attribute this difference in κ to the intrinsic electrical transport characteristics of nanotubes we have used (CoMoCAT batch SG65), which were predominantly semiconducting with a small amount of metallic nanotubes. The electrical transport properties of the aerogels can be tuned by varying the ratio of metallic versus semiconducting nanotubes. We have recently prepared aerogels with a different type of nanotubes (CoMoCAT CG100) containing both metallic and semiconducting nanotubes; κ for these aerogels were ≈250 S m^{-1} for ρ = 10 mg mL^{-1} which was similar to reported κ of other SWCNT foams.[17] The normalized electrical resistance (R/R_0) decreased dramatically (≈50%) with an increase in compressive strain to ≈15% but showed much smaller decrease (≈15%) with an increase in compressive strain from ≈15% to 60% (Figure 4b); here R is the electrical resistance and R_0 is the electrical resistance at compressive strain of 0%. We suggest that the nanotubes within the aerogels freely rotated about the existing nodes when compressed by ≈15% which increased contact area between nanotubes and drastically reduced electrical resistance (Figure 4b). As aerogels were compressed further, the nanotubes aligned and further increased the contact area between existing nodes and formed "new" nodes, which caused a gradual decrease in the resistance.

To characterize the mechanical properties, we measured compressive (tensile) stress (σ) as a function of compressive (tensile) strain (ε) for aerogels with ρ = 7.3–18.5 mg mL^{-1}. Representative plots of σ versus ε from compression and tensile loading for aerogels of ρ = 9.9 mg mL^{-1} are shown in Figure 4c. The high porosity of aerogels allowed compression of ≥90%. The Poisson's ratio (γ) of the aerogels, measured via compression loading on a cylindrical aerogels, at all ρ studied was very close to 0 for ε up to 60% (Supporting Information Figure S3), presumably because the highly porous structure of the aerogels with filamentous cell wall allowed compaction along compression direction without expansion normal to the compression

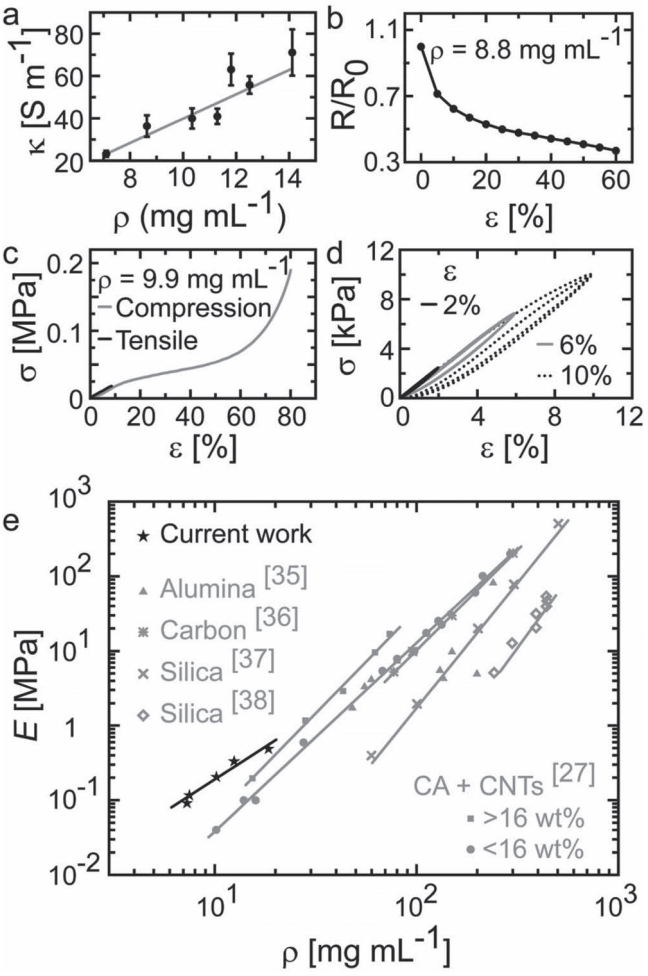

Figure 4. Electrical and mechanical properties of the aerogels. a) Aerogels were electrically conducting which suggests that aerogel fabrication did not damage nanotubes. b) R/R_0 decreased dramatically (≈50%) with an increase in ε to ≈15%. The decrease was much smaller (≈15%) for increase in ε from ≈15% to 60%. c) Stress (σ) vs strain (ε) of aerogels under compression showed three distinct regions: Hookian, plateau, and densification. The Young's moduli (E) for tensile and compressive loading were similar. d) Even in the Hookian regime, the aerogels plastically deformed when compressed for more than 2–3 cycles. The plastic deformation became more pronounced near ε = 9%. e) E of our aerogels at low density were larger than E of other reported aerogels. E of these aerogels had a power law dependence of ≈2 on ρ, which further confirmed the open-cell structure of the aerogels.

direction. Note that the slightly negative values of γ was probably an artifact of experimental errors in the measurements. The σ versus ε curves during compressive loading of aerogels at all ρ showed three characteristic deformation regimes typically observed for open-cell foams:[8] a Hookean or linear elastic regime (ε < 9%), a plateau region (9% ≤ ε ≤ 60%), and a densification region (ε ≥ 60%) with σ rising steeply (Figure 4c); the σ- and ε-ranges associated with different deformation regimes varied slightly with ρ of the aerogels. The permanent deformation of the aerogels for ε ≥ 9% hindered measurement of σ versus ε during the unloading cycle. The aerogels also showed plastic deformation within the linear elastic regime when compressed for more than 2–3 cycles, particularly at ε closer to 9% (Figure 4d). In tensile measurements, σ increased linearly with an increase in ε up to 9% when the aerogels cracked similar to a brittle material (Figure 4c). The compressive and tensile Young's moduli (E), calculated from the linear region of the σ versus ε curves (ε < 9%), were very similar for aerogels with the same density, likely a manifestation of isotropic orientation of nanotubes within the aerogels.[8] For example, compressive modulus for aerogels of ρ = 9.9 mg mL^{-1} (≈0.22 MPa) was very similar to tensile modulus (≈0.21 MPa). The Young's modulus increased with an increase in ρ with a power-law dependence of ≈2 (Figure 4e), further confirming that the aerogels had open-cell like structure.[8] At this low-density regime, our aerogels had the highest E compared to other types of aerogels (Figure 4e).[32–36] The storage (E') and loss (E'') moduli of the aerogels were nearly independent of frequency (ω) over the three decades of accessible ω-range of 0.4–400 rad s^{-1} (Supporting Information Figure S4).

We compared experimentally determined compressive plateau stress (σ_{pl}) to the maximum stress the aerogels can withstand due to the nodes between nanotubes (σ_{node}) and to the Euler buckling stress ($\sigma_{buckling}$) to gain insight into deformation mechanism of aerogels. We estimated σ_{node} as: $\sigma_{node} \approx \nu E_{interaction}$ where ν was the number of nodes per unit volume within the aerogels at a particular ρ and $E_{interaction}$ was the van der Waals interaction energy between nanotubes at the nodes.[25] We took $E_{interaction} \approx 40 k_B T$ where k_B is the Boltzmann constant and T is the temperature.[25] We calculated the number of nodes per nanotube by dividing length of a nanotube (≈1 μm) by the average distance between the nodes, ξ. For aerogels with ρ = 9.9 mg mL^{-1}, $\xi \approx 12$ nm[25] and the number of nodes per nanotube was ≈83, resulting in $\nu \approx 1.5 \times 10^{17}$ nodes cm^{-3} and $\sigma_{node} \approx$ 0.03 MPa. For aerogels with ρ = 9.9 mg mL^{-1}, the measured $\sigma_{pl} \approx$ 0.02 MPa (Figure 4c). Thus, we believe that the nanotubes in the aerogels bent in the Hookian regime resulting in linear elastic deformation and that the plateau regime started when the nodes between the nanotubes started to break. We also note that the actual stress on nanotubes at $\varepsilon \approx$ 9%, $\sigma_{crit} \approx \sigma_{pl}/\phi_{aerogel}$ was comparable to or exceeded the Euler buckling stress[8] for nanotubes: $\sigma_{buckling} = E_{nanotube} I/\xi^4$ at all ρ, where $\phi_{aerogel}$ was the volume fraction of aerogels, $E_{nanotube}$ was the Young's modulus of nanotubes ≈1.25 TPa,[10] I was the the second moment of inertia $= \pi D_{nanotube}^4/64$, $D_{nanotube}$ was the diameter of nanotubes. For example, aerogels with ρ = 9.9 mg mL^{-1} corresponded to $\phi_{aerogel} \approx 0.0076$ by taking density of a nanotube to be 1.3 g mL^{-1}. Then, $\sigma_{crit} \approx$ 0.02 MPa/0.0076 ≈ 2.63 MPa was comparable to $\sigma_{buckling} \approx$ 2.95 MPa, where we again took $\xi \approx$ 12 nm for $\phi_{aerogel} \approx 0.0076$.[25] It is possible that nanotubes also started to buckle in the plateau regime. We also believe that the aerogels could not recover their original shapes when compressed by 10–15% because of an absence of any restorative force that can disrupt any additional nodes formed between nanotubes at higher compression.

2.4. Thermal Management Characteristics of SWCNT Aerogels

Although the thermal conductivity (k) of aerogels was expected to be low due to ultra-low material content and thermal contact

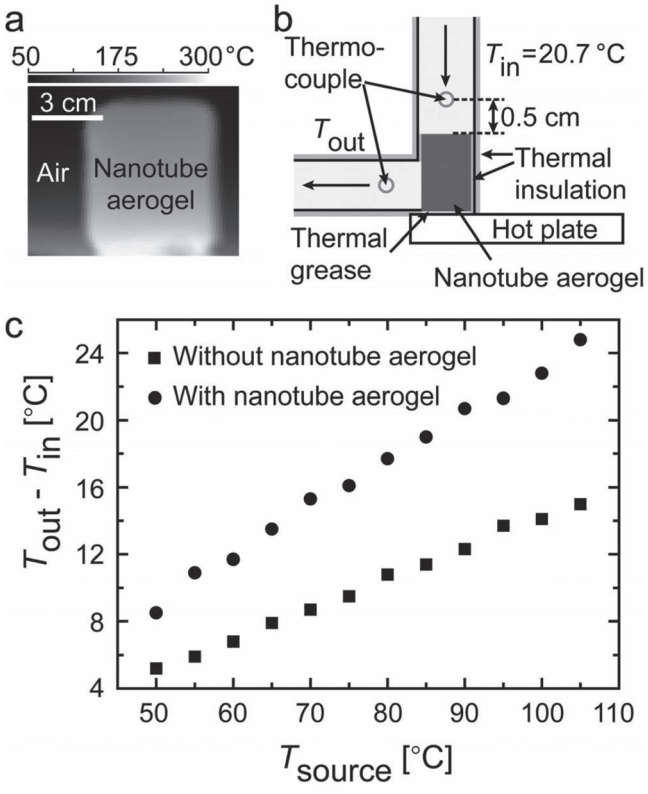

Figure 5. Thermal management characteristics of aerogels. a) Temperature profile obtained via infrared imaging showed that aerogels enhanced heat conduction through air. b) Schematic of a home-built system to measure heat transfer from a hot plate using aerogels as heat sinks using a forced convective cooling method. c) Temperature differences between the outlet (T_{out}) and inlet (T_{in}) air with and without an aerogel as heat sink on top of a hot plate at a surface temperature T_{source} showed potential of these aerogels as heat sinks.

resistance at the nodes,[37] we examined their heat conduction and heat transfer characteristics because of their large porosity, ultrahigh SSA and because individual SWCNTs have extremely large k, which have been reported to be ≥1000 W (m K)$^{-1}$.[12] For all thermal management characterization experiments, we used aerogels with ρ = 7.3 mg mL^{-1} (i.e., porosity: 99.4% based on $\phi_{aerogel}$) since these aerogels had the highest SSA (1291 m^2 g^{-1}) and the largest porosity.

We first investigated heat conduction through aerogels under natural convection in ambient conditions and in steady-state (details in the Experimental Section). Infrared imaging of the temperature profile of aerogels showed that the top of the aerogel reached ≈180 °C when the aerogels were in thermal contact with a hot stage at a surface temperature of 300 ± 0.45 °C (**Figure 5**a). In comparison, air temperature at the same height above the hot stage reached only ≈50 °C without aerogels. Interestingly, the temperature profile were not altered or enhanced with the addition of thermally conducting grease (between the stage and the aerogel), which suggested that the aerogels conformed to the stage surface morphology.

We examined the heat transfer potential of aerogels using an impinging-jet (i.e., a forced convective cooling) method[38] in an ambient environment at steady-state (setup and parameters in Figure 5b and Experimental Section). We note that the inlet air flow rate ($\dot{m}$ = 10 standard cubic centimeter, sccm) was sufficiently low that a flow restricting mask did not significantly improve the heat transfer from the hot surface, and was not used. Figure 5c shows the steady-state temperature difference between the outlet air (T_{out}) and the inlet air in an ambient environment (T_{in} = 20.7 °C) impinged upon a hot plate at a surface temperature T_{source} with and without aerogels as a heat sink. We then estimated the heat dissipation rate, q, with and without aerogels using the expression: $q = \dot{m}C_p(T_{in} - T_{out})$ where C_p is specific heat of air at a temperature = $(T_{in} + T_{out})/2$.[38] The aerogel enhanced the heat dissipation rate from the hot plate by ≈85% at low T_{source}, but the enhancement decreased slightly to ≈65% at high T_{source}.

3. Conclusions

We have fabricated free-standing aerogel monoliths composed of isolated SWCNTs. The extremely high SSA of the aerogels reached 1291 m^2 g^{-1}, which is close to the theoretical limit. The Young's modulus of these aerogels is larger than any other existing aerogels at comparable density. The aerogels greatly enhanced heat transfer compared to air in forced convective cooling method, likely from the high porosity and SSA of the aerogels. The tunability of the shapes and sizes of the aerogels coupled with solution based manipulation of nanotubes including removal of impurities and sorting by length, diameter and electronic properties, will make these aerogels suitable in a variety of applications including sensors, electrodes, heat sinks, fillers in composites[39,40] and membranes.

4. Experimental Section

SWCNT Aerogel Fabrication: Purified CoMoCAT SWCNTs (batch SG65; SouthWest NanoTechnologies, Inc.), which had diameters ≈ 0.8 ± 0.1 nm, lengths ≈ 450 nm-1 µm, were used, resulting in an aspect ratio ≈1000 (manufacturer's specifications).[41,42] Nanotubes were suspended in Millipore-filtered deionized water at a concentration of 0.1 wt% using sodium dodecylbenzene sulfonate (SDBS) surfactant (Acros Organics) at a SWCNT:SDBS ratio of 1:5 or 1:10;[23,24] different SWCNT:SDBS ratios did not result in any noticeable differences in aerogel quality. Suspensions were sonicated using a tip sonicator (Thermo Fisher 500) for 2 h at 60 W followed by centrifugation at 21 000 g for 30 min (Beckman Coulter Allegra 25R) to sediment nanotube bundles. The collected supernatants contained mostly isolated nanotubes. The nanotube concentration in the supernatants was determined using optical absorbance using UV-visible (vis)-near IR (NIR) spectrometer (Varian Cary 5000) with an extinction coefficient of 2.6 (absorbance mL) (mg mm)$^{-1}$ at 930 nm and the Lambert-Beer equation. Supernatants showed sharp van Hove peaks in the vis-NIR absorption and NIR fluorescence spectra indicating that our dispersion process did not cut or open the ends of nanotubes.[41] This was further supported by electrical conduction of the nanotubes.[41] The supernatants were then concentrated by evaporating water off to a final concentration of 3.5 to 4.5 mg mL^{-1}. In a previous work, small angle neutron scattering was used to show that nanotubes did not form bundles when densified to these high concentration dispersions.[26] The concentrated nanotube suspensions were degassed to remove any bubbles (bubbles significantly degrade the mechanical integrity of aerogels) and poured into various shaped molds. Nanotube suspensions formed hydrogels within 12 h due to van der Waals interactions between

nanotubes.[25,26] To remove SDBS from the hydrogels, a wash with 1 M nitric acid at 50 °C for 20 min was used. The acid wash did not damage nanotubes since Raman spectra from hydrogels before and after acid wash was nearly identical (Supporting Information Figure S5a). Note that surfactant removal by hot water induced a significant shrinkage of hydrogels[23] and was avoided. The acid-washed hydrogels were neutralized by washing with deionized water until pH equilibrated to 7. To create aerogels, water was exchanged with ethanol by sequentially soaking the surfactant-free hydrogels in ethanol baths (ranging from 20–100 vol% anhydrous ethanol) with a step size of 20% for 48 h at room temperature and then ethanol was removed from the hydrogels via critical-point-drying (CPD) (Autosamdri 815, Tousimis). Energy dispersive X-ray (EDX) spectroscopy showed that sodium and sulfur were not present in the aerogels (Supporting Information Figure S5b); the quantitative analysis limit of EDX was <1 wt%. Since sodium and sulfur are a component of SDBS, this suggested that the final aerogels were essentially surfactant-free. ≈10% shrinkage was observed along each dimension of the aerogels compared to the dimensions of the hydrogels. ρ of the aerogels was calculated based on the final mass and dimensions of the aerogels. Aqueous dispersions created from powdered aerogels clearly showed van Hove peaks in vis-NIR absorbance (Supporting Information Figure S5c) and NIR fluorescence spectra (Supporting Information Figure S5d). These spectra were similar to the spectra obtained from nanotube suspensions before hydrogel formation, confirming that nanotubes remained well-preserved through the aerogel fabrication process.

Raman Spectroscopy: Raman spectra were collected using an inverted Raman confocal microscope (inVia Raman microscope, Renishaw) with a 20× (0.4 NA) objective (Leica Microsystems) and a laser of wavelength 785 nm (1.58 eV). Laser power was set to 10 mW to avoid heat induced damage to the samples, and the laser spot size was 1–2 μm with an exposure time of 3 s. 10 scans were collected, each at five different locations for each sample, and the scans were averaged to improve signal-to-noise ratio. The data collection and analysis were performed using WiRE software (Renishaw). Each Raman spectrum was normalized by its G-band intensity.

Near-Infrared Fluorescence Spectroscopy: Near-infrared fluorescence spectroscopic characterization of dispersions prepared from powdered aerogels were collected using a Nanolog Spectrofluorometer system (Horiba Jobin Yvon) equipped with a liquid nitrogen cooled InGaAs array detector. NIR fluorescence data was analyzed using Nanosizer software (Horiba Jobin Yvon).

Electron Microscopy: The 3D networks of nanotubes within the aerogels, the pore radii and the pore structures were imaged using a scanning electron microscope (SEM; FEI Quanta 600) and a transmission electron microscope (TEM; FEI Tecnai F20) at 200kV. A Tecnai F20 at 200 kV was used to collect low resolution TEM images and an FEI Titan 83 at 300 kV to collect high resolution TEM (HRTEM) images.

Characterization of SSA, Pore Volumes, Pore Radii and Pore Radii Distribution: Aerogel SSA was measured by adsorption and desorption of nitrogen at 77 K using a BET surface area measurement system (Quantachrome NOVA 2000). The pore volumes and the pore radii distributions were then determined from the measured isotherms at 77 K using the NLDFT and BJH methods.

Electrical Resistance Measurements: Copper wire leads were attached to the flat surfaces of the cylindrical aerogels with silver paste (DuPont 4929N) and a two-probe contact direct current measurements using EC-Lab V10 and Fluke Ohmmeter were used to measure resistance of aerogels versus ρ.

Measurement of Mechanical Properties: The compressive and tensile measurements of σ as a function of ε were performed using an Instron 5940 series tabletop testing system with a 10 N load cell. The instrument had a position control resolution of <0.1 μm and could measure positions with an accuracy of 0.1% of displacement. For compressive measurements, cylindrical aerogel samples of diameter of ≈5 mm and length of ≈3 mm were loaded between two compression heads with the top head applying uniaxial compression and release on the sample along the vertical direction at speed of 1 mm min^{-1}. A 2% prestrain was applied to make a uniform flat contact between the compression heads and the sample and to prevent slipping of the sample. Since the aerogels were too fragile to hold using grips typically used for tensile measurements, cylindrical aerogel samples of diameter of ≈5 mm and length of ≈3 mm were attached to tensile heads using silver paste (DuPont 4929N) and left overnight for a complete curing of the silver paste before performing any measurements. No prestress was applied for tensile measurements and heads traveled at a speed of 1 mm min^{-1}. E' and E'' of aerogels were measured as a function of ω with a prestrain of 3% and an oscillatory compressive strain of 1% using a dynamic mechanical analysis system (G2-RSA, TA Instruments) and disk-shaped stainless steel compression heads of diameter 15 mm. Aerogels used for dynamical mechanical analysis ≈5.5 mm in diameter and ≈6.6 mm in length.

Thermal Management Characterization: Aerogels with $\rho = 7.3$ mg mL^{-1} (i.e., porosity ≈99.4% based on $\phi_{aerogel}$) were used for all thermal management characterization experiments since these aerogels had the highest SSA (1291 m^2 g^{-1}) and the largest porosity. For heat conduction experiments, aerogels of diameter and length of ≈5.5 mm and ≈6.6 mm, respectively, were placed on a digital hot plate (Corning) under natural convection and in ambient environment. The surface temperature of the hot plate was set using its high precision temperature controller to 300 ± 0.45 °C. A steady state temperature profile in the aerogel reached within ≈15 min. The temperature profile was imaged using an IR imaging camera (HotFind-V, Guangzhou SAT Infrared Technology). The temperature profile did not change significantly if thermally conducting grease (Cool Grease 7018, Melcor) was used between the aerogel and the hot stage.

The heat transfer characteristics were measured from a hot place with and without aerogels as heat sinks in ambient conditions and in steady-state using a home-built system based on a impinging-jet or a forced convective cooling method. The schematic of the system is shown in Figure 5b. The diameters of the inlet and outlet tubes were 5.6 mm, and they were enclosed within a Styrofoam tube coated on the outside with thermally insulating vacuum grease (Dow Corning) to reduce unaccounted heat loss. An aerogel of diameter and length of ≈5.5 mm and ≈6.6 mm, respectively, was placed at the bottom of the inlet tube and on a thermoelectric heating/colling stage (Melcor); a thermally conducting grease (Cool Grease 7018, Melcor) was used between the aerogel and the hot stage. Air at ambient temperature (T_{in} = 20.7 °C) was flowed through the inlet tube at a mass flow rate of 10 standard cubic centimeter (sccm); the air flow was controlled with a flow regulator. The inlet air flow rate was very low and air hit the hot plate. A flow restricting mask did not significantly improve the heat transfer from the hot surface and was not used. Since the aerogel had a slightly smaller diameter than the inner diameter of the inlet tube, this gap was closed using thermally insulating vacuum grease (Dow Corning) to stop air from flowing around the aerogel. The surface temperature of the hot stage was set using a high precision temperature controller (MTTC-1410, Melcor) from T_{source} = 50 ± 0.1 °C to 105 ± 0.1 °C. The outlet and inlet temperatures were measured using K-type beaded thermocouples (Thermo Fisher) placed 0.5 cm away from the perimeter of the aerogel and Traceable dual-channel thermometer (Thermo Fisher). The outlet temperature T_{out} reached steady-state within ≈15 min and was recorded. For comparison, the experiments were repeated keeping all parameters the same and without any aerogel.

Supporting Information

Supporting Information is available from the Wiley Online Library or from the author.

Acknowledgements

This work was supported by the NSF through grants DMR-0645596, CBET-0933510 & DMR-0619424, the Sloan Foundation, the American

Chemical Society Petroleum Research Fund, and the Korea Institute of Energy Research.

Received: April 17, 2012
Published online: August 27, 2012

[1] R. A. Vaia, H. D. Wagner, *Mater. Today* **2004**, *7*, 32.
[2] K. I. Winey, R. A. Vaia, *MRS Bull.* **2007**, *32*, 314.
[3] X. He, D. Antonelli, *Angew. Chem. Int. Ed.* **2002**, *41*, 214.
[4] L. J. Gibson, *Annu. Rev. Mater. Sci* **2000**, *30*, 191.
[5] J. A. Fernández, T. Morishita, M. Toyoda, M. Inagaki, F. Stoeckli, T. A. Centeno, *J. Power Sources* **2008**, *175*, 675.
[6] Y. Zhu, S. Murali, M. D. Stoller, K. J. Ganesh, W. Cai, P. J. Ferreira, A. Pirkle, R. M. Wallace, K. A. Cychosz, M. Thommes, D. Su, E. A. Stach, R. S. Ruoff, *Science* **2011**, *332*, 1537.
[7] N. C. Hilyard, A. Cunningham, *Low Density Cellular Plastics, Physical Basis of Behavior*, Chapman and Hall, London, UK **1994**.
[8] L. J. Gibson, M. F. Ashby, *Cellular Solids, Structure and Properties*, Pergamon, New York **1997**.
[9] A. Peigney, C. H. Laurent, E. Flahaut, R. R. Bacsa, A. Rousset, *Carbon* **2001**, *39*, 507.
[10] M. Treacy, T. Ebbesen, J. Gibson, *Nature* **1996**, *381*, 678.
[11] T. W. Ebbesen, H. J. Lezec, H. Hiura, J. W. Bennett, H. F. Ghaemi, T. Thio, *Nature* **1996**, *382*, 54.
[12] S. Berber, Y.-K. Kwon, D. Tomanek, *Phys. Rev. Lett.* **2000**, *84*, 4613.
[13] C. M. Yang, K. Kaneko, M. Yudasaka, S. Iijima, *Nano Lett.* **2002**, *2*, 385.
[14] M. Cinke, J. Li, B. Chen, A. Cassell, L. Delzeit, J. Han, M. Meyyappan, *Chem. Phys. Lett.* **2002**, *365*, 69.
[15] F. Li, Y. Wang, D. Wang, F. Wei, *Carbon* **2004**, *42*, 2375.
[16] Y. F. Yin, T. Mays, B. McEnaney, *Langmuir* **1999**, *15*, 8714.
[17] D. N. Futaba, K. Hata, T. Yamada, T. Hiraoka, Y. Hayamizu, Y. Kakudate, O. Tanaike, H. Hatori, M. Yumura, S. Iijima, *Nat. Mater.* **2006**, *5*, 987.
[18] A. Cao, P. L. Dickrell, W. G. Sawyer, M. N. Ghasemi-Nejhad, P. M. Ajayan, *Science* **2005**, *310*, 1307.
[19] J. Suhr, P. Victor, L. Ci, S. Sreekala, X. Zhang, O. Nalamasu, P. M. Ajayan, *Nat. Nanotechnol.* **2007**, *2*, 417.
[20] A. E. Aliev, J. Oh, M. E. Kozlov, A. A. Kuznetsov, S. Fang, A. F. Fonseca, R. Ovalle, M. D. Lima, M. H. Haque, Y. N. Gartstein, M. Zhang, A. A. Zakhidov, R. H. Baughman, *Science* **2009**, *323*, 1575.
[21] X. Gui, J. Wei, K. Wang, A. Cao, H. Zhu, Y. Jia, Q. Shu, D. Wu, *Adv. Mater.* **2010**, *22*, 617.
[22] M. Xu, D. N. Futaba, T. Yamada, M. Yumura, K. Hata, *Science* **2010**, *330*, 1364.
[23] M. B. Bryning, D. E. Milkie, M. F. Islam, L. A. Hough, J. M. Kikkawa, A. G. Yodh, *Adv. Mater.* **2007**, *19*, 661.
[24] M. F. Islam, E. Rojas, D. M. Bergey, A. T. Johnson, A. G. Yodh, *Nano Lett.* **2003**, *3*, 269.
[25] L. A. Hough, M. F. Islam, P. A. Janmey, A. G. Yodh, *Phys. Rev. Lett.* **2004**, *93*, 168102.
[26] L. A. Hough, M. F. Islam, B. Hammouda, A. G. Yodh, P. A. Heiney, *Nano Lett.* **2006**, *6*, 313.
[27] S. Brunauer, P. H. Emmett, E. Teller, *J. Am. Chem. Soc.* **1938**, *60*, 309.
[28] S. Brantiley, N. P. Mellott, *Am. Mineral.* **2000**, *85*, 1767.
[29] P. Tarazona, *Phys. Rev. A* **1985**, *31*, 2672.
[30] E. P. Barrett, L. G. Joyner, P. P. Halenda, *J. Am. Chem. Soc.* **1951**, *73*, 373.
[31] S. J. Gregg, K. S. W. Sing, *Adsorption, Surface area, and Porosity*, Academic Press, New York **1992**.
[32] M. A. Worsley, S. O. Kucheyev, J. H. Satcher Jr., A. V. Hamza, T. F. Baumann, *Appl. Phys. Lett.* **2009**, *94*, 073115.
[33] S. O. Kucheyev, T. F. Baumann, C. A. Cox, Y. M. Wang, J. H. Satcher, A. V. Hamza, J. E. Bradby, *Appl. Phys. Lett.* **2006**, *89*, 041911.
[34] N. Leventis, C. Sotiriou-Leventis, G. Zhang, A. M. Rawashdeh, *Nano Lett.* **2002**, *2*, 957.
[35] R. W. Pekala, C. T. Alviso, J. D. Lemay, *J. Non-Cryst. Solids.* **1990**, *125*, 67.
[36] T. Woignier, J. Reynes, H. Alaoui, I. Beurroies, J. Phalippou, *J. Non-Cryst. Solids.* **1998**, *241*, 45.
[37] M. B. Bryning, D. E. Milkie, M. F. Islam, J. M. Kikkawa, A. G. Yodh, *Appl. Phys. Lett.* **2005**, *87*, 161909.
[38] W. H. Hsieh, J. Y. Wu, W. H. Shih, W. C. Chiu, *Int. J. Heat Mass Transfer* **2004**, *47*, 5149.
[39] K. H. Kim, M. Vural, M. F. Islam, *Adv. Mater.* **2011**, *23*, 2865.
[40] K. H. Kim, Y. Oh, M. F. Islam, *Nat. Nanotechnol.* DOI: 10.1038/NNANO.2012.118.
[41] D. E. Johnston, M. F. Islam, A. G. Yodh, A. T. Johnson, *Nat. Mater.* **2005**, *4*, 589.
[42] M. F. Islam, D. E. Milkie, O. N. Torrens, A. G. Yodh, J. M. Kikkawa, *Phys. Rev. B* **2005**, *71*, 201401.